



Holistic determination of physical fracture toughness values and numerical parameters for delamination analysis considering multidirectional-interfaces

O. Völkerink^{a,*}, J. Koord^a, E. Petersen^b, C. Hühne^a

^a German Aerospace Center (DLR), Institute for Composite Structures and Adaptive Systems, Braunschweig, Germany

^b Fraunhofer Institute for Wind Energy Systems (IWES), Am Seedeich 45, 27572 Bremerhaven, Germany

ARTICLE INFO

Keywords:

Fibre reinforced materials
Delamination
Finite element analysis
Toughness testing
R-curve tests
Cohesive zone modelling
Interface fracture
Mixed mode fracture
R-curves
Damage tolerance

ABSTRACT

Delaminations are a concern for the structural integrity of fibre composite structures. The decisive material parameter for delaminations is fracture toughness. Structures usually have a multidirectional ply stacking. However, interface orientation dependant fracture toughness values and R-curve effects are neglected in numerical delamination analysis. This work investigates interface orientation specific fracture toughness values and considers R-curve effects in mode I to improve simulation accuracy. Therefore, mode I, mode II and mixed mode fracture toughness values of different interface ply orientations are determined experimentally and verified using numerical analysis of the characterisation specimens with cohesive zone modelling. In this way, an engineering methodology is provided for the experimental characterisation and comprehensive numerical modelling of delaminations in mesoscale progressive damage analysis of multidirectional composite structures. In addition, a full parameter set for the simulation of four different interfaces of M21-T700GC prepreg material is given. It can be shown that the use of standard $0^\circ//0^\circ$ -values leads to very conservative results. The use of interface specific values increases the accuracy. Ultrasonic scans of the DCB specimens are used to compare the crack front shapes for validation. Not only the load displacement curves of the characterisation specimens are well captured, but also the crack front shapes. This demonstrates that by smearing the microscale effects, the material behaviour can be captured phenomenologically correct by mesoscale modelling suitable for industrial use.

1. Introduction

Carbon fibre reinforced plastics (CFRP) show very high strength and stiffness to density ratios, what makes them often the preferred choice of material in lightweight engineering. On the contrary, they suffer from a low resistance against impacts and high risk of layer separation (delamination), leading to loss of stiffness and load carrying capacity. Therefore, an analysis has to be performed to determine the risk of delamination and guarantee the structural integrity of the composite structure.

Fig. 1 shows the possible fracture modes, caused by different load cases. Mode I represents crack growth under peel loading, where the crack propagates perpendicular to the loading direction. Crack growth parallel to the direction of loading is caused by shear in mode II. The fracture mode III is also caused by shear with crack growth occurring transversely to the direction of loading. Combinations of the individual modes are possible. They are referred to as mixed mode.

An established method for CFRP to determine failure loads is the use of critical energy release rates (cERR). According to Griffith [1],

the loss of energy per area is assumed to be an inherent material characteristic value G_c . These G_c values can be determined from static crack propagation experiments with beam type specimens and artificial pre-cracks.

To represent nearly pure fracture modes and characterise the respective fracture resistance, several static experiments have been established for use with unidirectional CFRP. The Double Cantilever Beam (DCB) test is the only standardised test for determining the cERR in mode I quantified as G_{Ic} [2]. In the DCB test, a peel load is applied directly to the crack, which is globally equivalent to a pure mode I load. However, if the upper and lower beams have different elasticity characteristics, local parasitic shear modes may occur [3]. In the experimental reproduction of pure mode II to determine G_{IIc} , the challenge is to apply the interlaminar shear load between the lower and upper arm of the specimen and thus correctly at the crack. Therefore, bending tests are usually considered, for instance the most commonly used 'End Notch Flexure' (ENF) test, which is also standardised [4]. In the ENF test a three-point bending setup is used and a moment creates

* Corresponding author.

E-mail address: oliver.voelkerink@dlr.de (O. Völkerink).

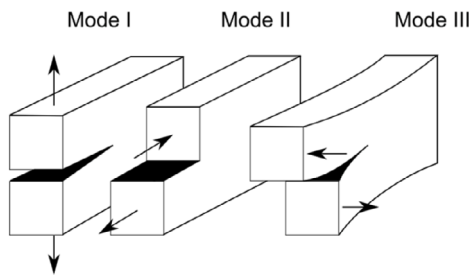


Fig. 1. Fracture modes under peel and shear loading in and normal to the plane of crack propagation.

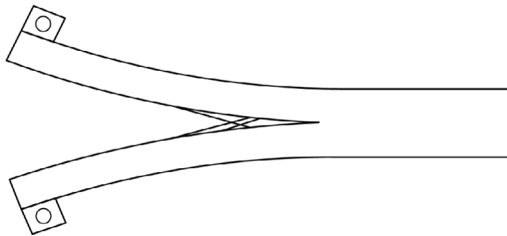


Fig. 2. Schematic illustration of fibre bridging in the DCB test.

a relative displacement between the upper and lower test specimen leading to shear in the interface.

However, pure Mode I or Mode II loads rarely occur in real structures, but mostly mixtures of the modes. In order to also be able to characterise the behaviour under these mixed mode loads, various experiments were developed in the past. Most tests have not gained acceptance because they either allow only a limited range of mixed mode ratios or the interpretation of the test data is difficult and requires FEM analyses [5]. For these reasons, the mixed mode bending (MMB) test from Crews and Reeder [6] has become popular because it allows the testing of any mixed mode ratio and is relatively easy to evaluate.

During crack growth, there may be an increase in the cERR, so that different values exist for crack initiation and propagation. This resistance or R-curve called behaviour originates from micromechanical processes. In particular, the bridging of the gap by individual fibre bundles causes an increase of the delamination resistance during crack propagation, as shown schematically in Fig. 2. The first, who investigated this behaviour were Johnson and Mangalgi [7]. They showed that an increase of fracture resistance is accompanied by an increase of fibre bridging. Especially in the case of interface layers of the same orientation, unidirectional 0° fibre bundles cause the layers to penetrate each other. However, R-curve behaviour is not a pure material property. In fact, it depends on the geometry of the test specimen. [8].

This leads to varying cERR for different layers adjacent to the interface, like occurring in multidirectional laminates. Composite layups are in general composed of laminas with varying orientation to adapt stiffness and strength in accordance with the main load directions. The delamination can occur between layers of different orientations as, in general, layers of 0° , 90° and $\pm 45^\circ$ orientations are used. Pereira et al. showed that G_{Ic} values depend on the orientation of the adjacent layers in the interface and higher values occur for $0^\circ//0^\circ$ interfaces than for $0^\circ//45^\circ$ and $0^\circ//90^\circ$ interfaces [3,9]. On the contrary, in mode II $0^\circ//0^\circ$ interfaces show lower G_{Ic} values than multidirectional interfaces [10]. Conflicting results are presented by Bienias [11], where G_{Ic} is observed to decrease with increasing ply angle difference. Andersons and König present a review of experimentally determined cERR for different interfaces of adjacent layers and external loading direction [12]. They state that G_{Ic} values of a unidirectional interface increases strongly with increase of loading direction from parallel to transverse loading to

fibre orientation, meaning an interface of $0^\circ//0^\circ$ has a lower fracture toughness than an $90^\circ//90^\circ$ interface. On the opposite, in mode II the unidirectional interface shows a small decrease of G_{Ic} with increase of the loading direction.

Two more recent studies from Blondeau et al. [13] and Yu et al. [14] investigate the R-curve behaviour of multidirectional carbon/epoxy prepreg laminates with different interface orientations under mode I loading. Both studies conclude that the steady state cERR is much more influenced than the initiation cERR. The work from Pichler et al. [14] is much more holistic since they investigate a carbon/epoxy prepreg material under mode I, mode II and mixed mode loading using DCB, 4ENF and MMB tests. The findings are regarding the cERR are comparable to those in [13,14]. However, they highlight that almost all studies examine behaviour in one mode only, but that there is a lack of studies that examine all relevant modes.

An explanation lies in the cERRs determined on macroscopical level. On this level an idealised fracture surface perpendicular to the adjacent layers is assumed. On micromechanical level a delamination shows different fracture characteristics as can be identified by scanning electron microscope [15]. Pure resin failure is combined with interface failure between fibres and resin. The crack follows the fibres, leading to a coarse and increased fracture surface. All the phenomena and especially the increased fracture surface are included in the macroscopical effective cERR leading to different G_c values for different combinations of adjacent layer orientation. As laminates in general are composed of layers with multidirectional orientations, the cERRs have to be determined for all possible layer combinations.

Investigations by Pereira et al. [3] have shown that without generating a natural pre-crack cERR in DCB experiments can be considerably lower for multidirectional interfaces. For unidirectional interfaces, on the other hand, no serious difference was found. In mode II, the resin accumulation at the ends of the foil can increase the crack resistance. This results in higher critical energy release rates for artificial pre-cracks, especially for $0^\circ//0^\circ$ interfaces [10]. However, the introduction of a natural mode II pre-crack is very difficult, since a total failure of the specimen can already occur due to sudden crack propagation. The otherwise common procedure of shortening a DCB test specimen and to use it as an ENF specimen is not possible for multidirectional laminates due to an inhomogeneous crack front and observed crack jumping.

For the investigation of multidirectional interfaces or those between different materials, an asymmetrical layout of the specimens is inevitable. This leads to undesired fracture modes in addition to the dominant fracture mode, which is especially caused by undesired torsion in $\pm 45^\circ$ -layers [10,16,17].

It is possible to consider the influence of the asymmetry on the mode ratio and to determine the individual mode portions [18,19]. To determine almost pure mode cERR values the influence of the asymmetry can be reduced by balanced layups, which have low laminate coupling terms [12,20]. Recommendations exist for specimens with multidirectional interfaces, which must be fulfilled for both the upper and the lower specimen arm. For the coupling of the bending terms, Prombut et al. [21] give the following limit:

$$D_c = \frac{D_{12}^2}{D_{11}D_{22}} \leq 0,25. \quad (1)$$

In addition, the bending-torsion coupling should fulfil the condition,

$$B_t = \left| \frac{D_{16}}{D_{11}} \right| \ll 1. \quad (2)$$

A special phenomenon in multidirectional specimens is so called “crack jumping” as e.g. investigated by Tao et al. [22] for mode II crack propagation. The crack leaves the interface under investigation by “jumping” transversely through an adjacent layer and continues in another interface. The intralaminar crack growth dissipates energy and after crack jumping the crack propagates in an undesired interface.

Hence, the determined cERR does not describe the fracture toughness of the interface intentionally under investigation. As Choi et al. [23] investigated for $45^\circ// -45^\circ$ interfaces, edge inserts could be used to prevent crack jumping. Recent studies from Garulli et al. investigate how undesired effects in fracture toughness tests can be minimised by so called fully uncoupled multidirectional layouts and present a procedure to determine these layouts [24–26].

In order to predict the onset of cracking in a complex composite structure and to be able to make a statement about crack propagation and remaining load carrying capacities, a sound simulation taking into account the identified fracture phenomenology is necessary. The presented study provides the required tools to perform such a delamination analysis on an multidirectional composite structure by meso-scale FE simulation. This includes the necessary full characterisation of cERRs under mode I, mode II and mixed mode loading of the different interfaces in multidirectional laminates for one specific carbon/epoxy prepreg material (M21-T700GC). Four different interfaces, including $0^\circ//0^\circ$, $0^\circ//45^\circ$, $0^\circ//90^\circ$, $+45^\circ// -45^\circ$, are investigated. Examinations of the R-curve behaviour is limited to mode I, since the chosen and most used 3ENF test prevents measuring the mode II R-curve due to unstable crack growth [27]. In addition, the fracture surfaces and crack paths as well as the crack front shapes are investigated and considered for validation of the simulation tools. Beside recognised fracture models an adapted trilinear cohesive model is implemented to capture R-curve behaviour in very precisely and computationally effective. Further, crack jumping is identified by a 3D failure criterion for the CFRP plies themselves. Thus, a complete set of parameters is available for each interface under investigation. Aim is to provide a validated set of parameters for each interface and the developed R-curve model for an effective fracture analysis of arbitrary complex composite structures.

2. Meso-scale numerical modelling approach

State-of-the-art for modelling delaminations in this kind of analyses are CZM [28], VCCT [29] and XFEM [30]. In this work the CZM is preferred because no initial crack is needed, it can be used as element- or surface-based behaviour, can model both initiation and propagation and has the possibility to model R-curve behaviour [31,32]. However, for evaluation of mode mixture, especially in the specimens with multidirectional layout and interfaces, some VCCT analyses are performed because the occurring ERRs are directly provided by Abaqus when using VCCT. XFEM is omitted because it is very costly in terms of computation time [30].

In the CZM approach, cohesive traction is associated with a separation at an interface where a discrete crack may occur. The damage is initiated, if a maximum interface strength, also called traction, is reached. The relationship of cohesive traction and the displacement at the interface is called traction–separation law. There are several different types of traction–separation laws mentioned in literature. Baseline in this work is a bilinear law which is combined to a trilinear law by superposition for relevant cases. The area under the traction–separation law is equal to the fracture toughness G_c of the interface [33].

For the use of CZM, regardless of element or surface-based, several numerical parameters must be chosen. The following sections describe the selected approaches to choose values for the different parameters.

2.1. Elastic behaviour

In CZM analyses the cohesive stiffness is a numerical parameter. Turon et al. [33] published an analytical solution to estimate the cohesive stiffness. The aim is that the effective elastic properties of the composite will not be affected by the cohesive behaviour. Otherwise the delamination onset would be delayed. This is given whenever $E_3 \ll K$, i.e.,

$$K = \frac{\beta \cdot E_3}{h} \quad \text{with} \quad \beta \gg 1, \quad (3)$$

where h is the half beam thickness of the adjacent sub-laminate, β the parameter to ensure compliance is much larger than 1 ($\beta \gg 1$) and E_3 is the stiffness of the laminate in thickness direction.

Overall structural stiffness is correctly modelled above a certain value of K . However, excessively high values of K , for instance 10^7 or 10^8 N/mm³, lead to significant oscillations in the loading behaviour during the delamination propagation process. These oscillations can result in over-predictions of the structural failure load [34].

The stiffness has a strong impact on computational efficiency since the stable time increment in explicit analyses is inversely proportional to the interface stiffness. Thus, the number of needed increments increases with higher stiffness. Therefore, the goal is to keep the interface stiffness as low as possible.

An overview of commonly used stiffness values is given by Lu et al. [34]. Values between 10^5 to 10^6 N/mm³ are appropriate candidate choices for carbon/epoxy composites, allowing for both accuracy and feasibility of the simulation. As a starting point $K = 10^5$ N/mm³ is chosen in this study. If necessary, it will be adjusted to higher values during calibration.

2.2. Interface strength and element edge length

In the following, it will be explained why the element size and the cohesive strength of the interface cannot be considered separately. Both depend on the cohesive zone length l_{CZ} . The physical l_{CZ} is defined as the length over which a degradation of the interface in front of the crack has occurred. Whereas the numerical l_{CZ} is defined by the length over which the interface elements are degraded in front of the crack. This means that they lie in the softening part of the traction–separation response [35].

The l_{CZ} depends on the mechanical parameters of the interface. In literature, different numbers are mentioned for the minimum required elements modelling the fracture process zone. Some authors state that at least two elements are required over the zone length, but others demand up to ten [33]. The majority of authors specify the required number of elements to at least three [33,35].

There are several equations to calculate the characteristic length of the numerical cohesive zone to determine the required element length of the mesh. The original equation for isotropic materials was developed by Hillerborg et al. [36] for the use of cohesive zone models in concretes:

$$l_{ch} = E \frac{G_c}{(\sigma_{max})^2} \quad (4)$$

Yang and Cox developed a modified version of Eq. (4) for orthotropic materials. E' is an equivalent elastic modulus for orthotropic materials which depends on the longitudinal, the transverse and the shear modulus as well as on the depth and whether plane stress or plane strain conditions are assumed [35,37]. A detailed description of its calculation can be found in Harper and Hallett [35]:

$$l_{ch,I} = E'_I \frac{G_{Ic}}{(\sigma_{I,max})^2} \quad (5a)$$

$$l_{ch,II} = E'_{II} \frac{G_{IIc}}{(\sigma_{II,max})^2} \quad (5b)$$

This version was further modified by the same authors for the use with slender laminates [37]:

$$l_{ch,slender,I} = \left(E'_I \frac{G_{Ic}}{(\sigma_{I,max})^2} \right)^{\frac{1}{4}} h^{\frac{3}{4}} \quad (6a)$$

$$l_{ch,slender,II} = \sqrt{\left(E'_{II} \frac{G_{IIc}}{(\sigma_{II,max})^2} \right) h} \quad (6b)$$

However, Yang and Cox do not give a definition of a slender body. Harper and Hallett [35] suggest to calculate the characteristic length

with both, normal orthotropic and the slender orthotropic, equations and then take the minimum value to be conservative.

As can be seen from the Eqs. (4) to (6b) the characteristic length and hence the maximum element size depends on the interface strengths σ_{max} . Interface strength is a difficult parameter to measure. Petersen et al. [38] derived from unfolding tests with L-profile specimens strengths $\sigma_{I,max}$ of 79 MPa to 94 MPa for the material considered in this work.

These values result in characteristic lengths of $l_{ch,I} = 0.36$ mm and $l_{ch,I} = 0.50$ mm and thus element lengths of $l_{el} = 0.12$ mm and $l_{el} = 0.17$ mm for three elements in the cohesive zone. For the mesoscale analysis of a coupon or even a structural detail as target application, these element lengths are too small to achieve reasonable computing times.

Element lengths of $l_{el} = 0.75$ mm to $l_{el} = 1.0$ mm can typically be found in mesoscale analysis using continuum damage mechanics approaches to model the intralaminar failure behaviour of the composite structure [39]. As an engineering solution, Turon et al. [33] propose the reduction of the strength, so that the cohesive zone becomes so large that even with the target element size, a minimum number of elements lie in the cohesive zone.

This can be justified by the fact that as soon as a crack is initiated and a cohesive zone exists in the structure, only the fracture toughness value is critically important. At this stage the results are relatively insensitive to the interface strength values [33]. This approach is also followed in this work. However, not the equation proposed by Turon et al. [33] but the Eqs. (4) to (6b) presented above are used to calibrate the interface strength. The correction factor M introduced by Harper and Hallett [35] to gain a close match between experimental and numerical results is not applied in this work since all results show a good agreement without scaling the element size further down.

The apparent interlaminar shear strength in mode II is determined by using short-beam-shear tests. The determined value of $\sigma_{II,max} = 110$ MPa has not to be reduced since the characteristic length is more than three times larger as the targeted element size.

2.3. Initiation criterion

The initiation of damage can be predicted using a stress-based quadratic power law as proposed by Ye [40]:

$$\left(\frac{T_I}{T^0}\right)^2 + \left(\frac{T_{II}}{T^0}\right)^2 + \left(\frac{T_{III}}{T^0}\right)^2 = 1 \quad (7)$$

The criterion was successfully applied in previous studies [28,41,42] and is also used in this work.

2.4. Propagation criterion

A crack propagates, if the ERR exceeds the fracture toughness or cERR. For pure modes the ERR can be compared to the determined cERR in this mode. Though, in real structures, a mixed mode loading conditions will occur. For that reason, a propagation criterion which includes the mode interaction is necessary. As discussed by Turon et al. [43] the power law criterion by Wu and Reuter [44] is the most widely used one:

$$\left(\frac{G_I}{G_{Ic}}\right)^\alpha + \left(\frac{G_{II}}{G_{IIc}}\right)^\alpha + \left(\frac{G_{III}}{G_{IIIc}}\right)^\alpha = 1 \quad (8)$$

However, Camanho et al. [28] state that the power law criterion is good for thermoplastic composites using $\alpha = 1$, it failed to describe the mixed mode fracture toughness of epoxy-based composites with $\alpha = 1$ and $\alpha = 2$. Much better suited for epoxy composites is the criterion by Benzeggagh and Kenane [5]. Therefore, it is used in this work.

$$G = G_{Ic} + (G_{IIc} - G_{Ic}) \left(\frac{(G_{II} + G_{III})}{(G_I + G_{II} + G_{III})} \right)^\eta \quad (9)$$

The interaction exponent η is determined with MMB tests in this work.

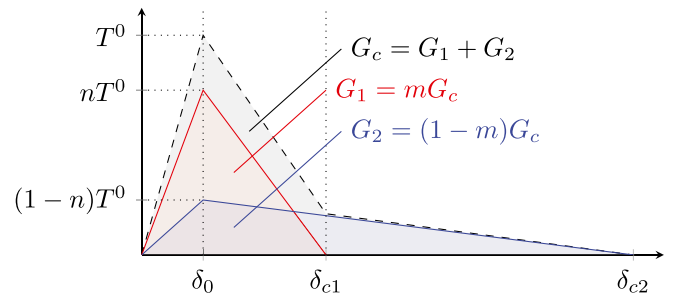


Fig. 3. Trilinear traction-separation-law obtained by superposing two bilinear laws.

2.5. Modelling R-curve behaviour

Davila et al. [32] showed that R-curve behaviour can be modelled by superposing two bilinear cohesive laws with different stiffnesses, interface strengths and fracture toughnesses. The superposition of two bilinear laws resulting in a trilinear law is shown in Fig. 3.

The two bilinear laws may be considered as representations of different phenomena. The first law with the subscript $_1$ has a high traction peak T^0_{n1} , a short critical opening displacement δ_{c1} and may be seen as representation of the quasi-brittle delamination fracture. The second bilinear law with subscript $_2$ can be regarded as a description of fibre bridging. It has a lower peak stress and a much longer critical opening displacement δ_{c2} compared to the first law. However, the two bilinear traction-separation laws are used for simplicity and do not necessarily correspond to two different failure modes that might peak at different displacement jumps. Actually, the bridging strength does not contribute significantly to the peak strength related to the intrinsic fracture process prior to fibre bridging. To obtain the characteristic values for the somehow pragmatic approach, the total interface strength T^0 and the total fracture toughness G_c are subdivided in the following manner:

$$T^0_1 = nT^0; \quad T^0_2 = (1-n)T^0 \quad (10)$$

$$G_1 = mG_c; \quad G_2 = (1-m)G_c \quad (11)$$

The stiffnesses are chosen in a way that the maximum tractions of both bilinear laws occur at the same separation. Several publications have proven that this approach is able to model R-curve behaviour in numerical analyses [32,45-48]. To add, de Morais proposes a closed-form analytical solution with a similar trilinear traction-separation law [49]. The difficulty arises in determining the parameters of the two traction-separation laws. Determination of m from the initial and the steady-state fracture toughness values is straightforward using the following Eq. from [46]:

$$m = \frac{G_1}{G_c} = \frac{G_{c-init}}{G_{c-ss}} \quad (12)$$

However, there is no commonly accepted approach to find n . In this study, the semi-empirical approaches of [32] were used first. Tough, this approach did not result in a satisfying correlation with the experiments. Airoldi et al. [46] performed several parametric analyses and minimised the error between averaged experimental and numerical force-displacement curves. In this study, as in the publications [47, 48], the determination of n is done by very simple means, through adjustment by testing or trial and error. The parameter n controls the interface strength T^0 . Higher values of n eliminate the pre-peak nonlinearity and vice-versa. For the specimens with $0^\circ/45^\circ$ interface the numerical results with two different values for n are shown in Fig. 10(b). Another approach is to modify the fracture toughness value with crack growth during simulation [50-52]. This approach is simpler in application because the values can be taken directly from the R-curves. In this way, it circumvents the lack of methods to calibrate



Fig. 4. DCB model for mode I parameter calibration.

the parameters of the superposed cohesive laws. Nevertheless, in this work the superposition approach is followed. The modelling of the R-curve behaviour is only one aspect of the holistic description of multidirectional interfaces and for the approach of for example Raimondo et al. [52] a user defined material model is required, which is beyond the scope of this work.

2.6. Simulation models

FE models are used to validate the determined fracture toughness values on the basis of experimental and numerical force–displacement curves. Furthermore, the mode mix, the shape of the crack front and the intralaminar material stressing efforts in the beams are investigated. For this reason, detailed 3D models with a layer-wise approach for the fibre composite are used. The analyses of the 3D model were solved explicitly using Abaqus/Explicit Version 2020.

The composite beams of the specimens are modelled with a layer-wise approach using reduced integrated 8-node linear solid elements (C3D8R) with an in-plane edge-length of 2.5 mm and one element per layer in through-thickness direction. In the region of interest the in-plane edge-length in crack growth direction is reduced to 0.75 mm. Deviating from this and following the recommendations from Darciik [53], a mesh refined to 0.25 mm by 0.25 mm in-plane edge length in the area around the crack is used for the VCCT analyses.

The composite beams are modelled as linear-elastic transversally isotropic material using the material data from Petersen et al. [54]. In this work the element-based CZM approach is used to model the delamination because the superposition of two bilinear traction–separation laws does not work with the surface-based approach in Abaqus. As previously described, the target element size lies between 0.75 and 1.0 mm. The previously described procedure results in a mode I interface strength of 20 MPa for the 0°//0° interface for the element edge length of 1.0 mm and three elements in the process zone. The mode II interface strength is set to the interlaminar shear strength of 110 MPa. If the element edge length is reduced to 0.75 mm, like in this study, these strengths result in four elements in the process zone. As the energy release rates of the other interface variants are higher, the process zones are larger and therefore modelled with more elements. Hence, the use of the 0°//0° values can be considered as a conservative approach.

The aluminium parts, where the hinges are attached to in the experiment, are also modelled with solid elements (C3D8R) and connected to the composite beams with tied contacts. The translatory degrees of freedom of the middle row of nodes on the upper aluminium part are locked. At the same node set the reaction forces are taken and summed up for evaluation. A displacement in loading direction is applied to the middle row of nodes of the lower aluminium part. The remaining two translatory degrees of freedom are locked. The model of the DCB specimen is shown in Fig. 4.

In the case of the ENF specimen, cf. Fig. 5, the translatory degrees of freedom are locked at the nodes of the lower outer edges. At these nodes also the reaction forces are taken for summation and evaluation. The pin, which moves down and applies the force to the specimen is modelled as rigid body. A displacement is applied in loading direction at the control point and the other two translatory degrees of freedom are locked. All other modelling is the same as for the DCB specimens.

The MMB specimen itself is modelled like the DCB specimen described above. In addition, a lever is modelled with shell elements

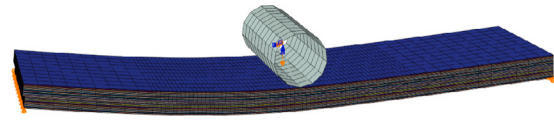


Fig. 5. ENF model for mode II parameter calibration.

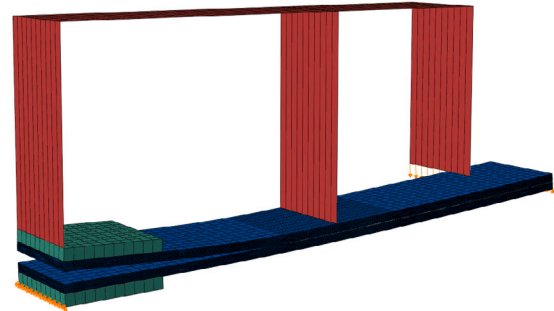


Fig. 6. MMB model for mixed-mode parameter calibration.

of very high stiffness to represent the movable part of the fixture. It is connected to the specimen via equation constraints, in which the translatory degrees of freedom are coupled. At the front edge of the lower load block the translatory degrees of freedom are locked. At the lower edge of the rear end the specimen is simply supported to simulate the bearing of the fixture. A displacement load is introduced at the lever edge representing the saddle of the fixture, cf. Fig. 6.

2.7. Evaluation of laminate stressing effort

As described before, crack jumping from the original plane, the plane with the pre-crack, to another interface could occur in the multidirectional specimens. This process implies that the crack migrates as a matrix crack from one interface to the other [55]. In order to assess the tendency to crack jumping, the material stressing effort is calculated in post for the plies adjacent to the original crack plane using the Failure Mode Concept (FMC) by Cuntze [39,54]. With the FMC the stressing efforts in five failure modes are calculated. These are FF1 and FF2 for fibre failure in tension and compression as well as IFF1 to IFF3 for interfibre failure in tension, compression and shear.

3. Analytical solutions

In this work, analytical solutions are used to verify the FE models and quickly determine trends due to the change in fracture toughness. As suggested in the corresponding ASTM standards, the Corrected Beam Theory (CBT) is used in this work. CBT corrects the displacement for shear deformation as well as for local deformations occurring around the crack tip. The following equations used for mode I and mode II are taken from Harper and Hallett [35].

$$\delta_I = \frac{2P(a + \chi h)^3}{3E_{11}I} \quad (13)$$

The tip displacement δ_I can be calculated using Eq. (13) in which P is the applied force, a is the crack length and h is the half beam thickness. Further, the stiffness E_{11} and the bending stiffness $I = Bh^3/12$ have to be considered. The parameter χ is calculated with:

$$\chi = \sqrt{\frac{E_{11}}{11G_{13}} \left[3 - 2 \left(\frac{\Gamma}{1 + \Gamma} \right)^2 \right]} \quad (14)$$

where Γ results from the following equation:

$$\Gamma = 1.18 \frac{\sqrt{E_{11}E_{22}}}{G_{13}} \quad (15)$$

With a linearly increasing tip displacement, the load P increases up to the point where $G_I = G_{IC}$. Then the crack starts to propagate and the load–displacement relationship for each increment of crack growth is found by combining the Eqs. (13) and (16), where G_I is set equal to G_{IC} .

$$P_I = \sqrt{\frac{G_I(a + \chi h)^2}{BE_{11}I}} \quad (16)$$

The analytical load–displacement curves for ENF and MMB are calculated in the same way. Only the equations for the tip displacement and the energy release rate change:

$$\Delta_{II} = \frac{3P(a + 0.42\chi h)^3 + 2PL^3}{96E_{11}I} \quad (17)$$

$$P_{II} = \sqrt{\frac{G_{II}64BE_{11}I}{3(a + 0.42\chi h)^2}} \quad (18)$$

The solution for MMB is taken from the ASTM D 6671-06 standard. The BK-criterion is used to calculate the cERR GT_c under mixed mode loading.

$$\Delta_{MM} = \frac{P_{MM}}{8bE_{11}h^3L^2} [4(3c-L)^2(a+h\chi)^3 + (c+L)^2(2L^3 + 3(a+0.42h\chi)^3)] \quad (19)$$

$$P_{MM} = \sqrt{\frac{\frac{4}{3}G_T b^2 E_{11} h^3 L^2}{(3c-L)^2(a+h\chi)^2 + \frac{3}{4}(c+L)^2(a+0.42h\chi)^2}} \quad (20)$$

The CBT equations are intended for the use with unidirectional laminates. To adapt the equations for the use with multidirectional laminates, in this work all specimens types except the one with $0^\circ//0^\circ$ -interface, homogenised properties from the ABD matrix of the laminates can be used. This is done using the Classical Lamination Theory. However, with CBT it is not possible to account for different properties of the lower and upper beam in case of non symmetric lay-ups [56]. The Extended Beam Theory (EBT) [16,17] does account for this effects and would probably provide better results. However, due to simplicity and because the stiffness of the chosen layups for upper and lower beam are nearly identical, the authors stick to CBT like recommended in the ASTM standards.

4. Experimental testing

4.1. Specimen manufacturing

Manufacturing of the DCB, ENF and MMB test specimens is done using unidirectional CFRP prepreg material by Hexcel (HexPly M21/35%134gsm/T700GC) with a nominal ply thickness of 0.13 mm. In order to investigate the interlaminar behaviour of multidirectional interfaces, the laminate stacking sequence needs to be adjusted. As discussed in Section 1, the resulting laminate layups are inevitably asymmetric. However, by employing laminate layups conforming to the conditions proposed by Prombut et al. [21] in Eqs. (1) and (2) parasitic ERR effects are reduced. The resulting laminate layups for the interfaces $0^\circ//0^\circ$, $0^\circ//45^\circ$, $0^\circ//90^\circ$ and $45^\circ//45^\circ$ are presented in Table 1. As can be seen, the requirements for D_c and B_I are well met, thus indicating minimised effects by parasitic modes.

The use of sub-laminates within the multidirectional specimens minimises coupling effects and generates nearly isolated fracture modes. The asymmetric layups of the $45^\circ//45^\circ$ sample originates from the investigation of edge effects in the DCB experiment [23,57]. The setups for $0^\circ//90^\circ$ and $0^\circ//45^\circ$ have also been successfully used in DCB and ENF experiments to determine the corresponding characteristic values [21,22].

The plates are laid by hand, vacuum sealed and cured in an autoclave using the manufacturer’s recommended cure cycle. The initial pre-crack is introduced into the laminate during the hand layup process by insertion of a double-layered PTFE foil of 25 μm in thickness.

Table 1

Laminate layups for multidirectional interface testing.

Interface	Layup	D_c [-]	B_I [-]
$0^\circ//0^\circ$	$[0_{34}]$	0.00647	0.00000
$0^\circ//45^\circ$	$[(0_2/90)_6/0_2// + 45/(0_2/90)_6/0_2]$	0.00191	0.00000
$0^\circ//90^\circ$	$[(0_2/90)_6/0_2/90/(0_2/90)_6/0_2]$	0.00191	0.00000
$45^\circ//45^\circ$	$[-45, 0, +45_2, 0, -45, +45, 0, -45_2, 0, +45// -45, 0, +45_2, 0, +45, -45, 0, -45_2, 0, +45]$	0.22293	0.00000

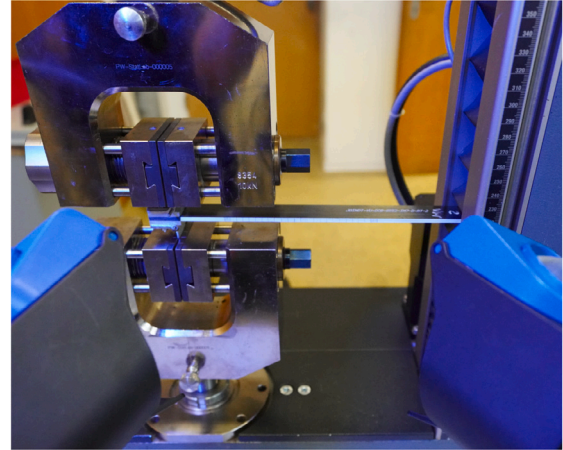


Fig. 7. DCB specimen inside fixture according to ASTM D5528.

Subsequent to the autoclave process, the specimens are cut to size using a diamond saw and measured with a caliper gauge. Manufacturing of the DCB and MMB specimens further requires application of load introduction elements according to ASTM D5528 and ASTM D6671. In the present case, piano hinges are bonded onto the ends of the specimens using a film adhesive. The last step in fabricating the DCB specimens consists in applying marks on the side of the DCB specimen for determination of the position of the crack tip during experimental testing. For this purpose, the side of the DCB specimen is coated with a thin layer of white chalk ink. Black lines indicating the distance from the initial crack tip are finally added. After manufacturing, all specimens are stored at $23 \pm 3^\circ\text{C}$ and $50 \pm 10\%$ rel. humidity until testing.

4.2. Test setup and procedure

Investigation of the mode I, mode II and mixed mode interlaminar behaviour of multidirectional interfaces is conducted using the DCB setup according to ASTM D5528, the ENF setup according to ASTM D7905 and the MMB setup according to ASTM D6671. The specimens are tested in a servo-mechanic testing machine by Zwick (Zwick 1484), which is equipped with a 20 kN load cell. The DCB setup in Fig. 7 is extended with a consumer fullframe mirrorless camera with a resolution of 42 megapixels and a spotlight in order to be able to analyse crack propagation during the DCB test. The setup allows to take pictures at a frequency of 1 Hz synchronised with the testing machine’s force and displacement output data for determination of R-curves after testing. As explained in Section 1, in case of DCB testing, a natural pre-crack is introduced in the delamination plane prior to the actual test. Therein, the DCB specimen is mounted inside the testing rig and the specimen halves are separated manually until the initial crack of 40 mm in length defined by the PTFE insert is increased by 3 mm to a total pre-crack length of 43 mm. After introduction of the natural precrack, the specimen halves are unloaded in order to conduct the actual DCB test at a constant crosshead speed of 1 mm/min.

In Fig. 8, an ENF specimen inserted inside a 3-point bend setup is shown. The specimen is supported by two bottom legs, while the bending load is introduced using the centre stamp at a constant crosshead

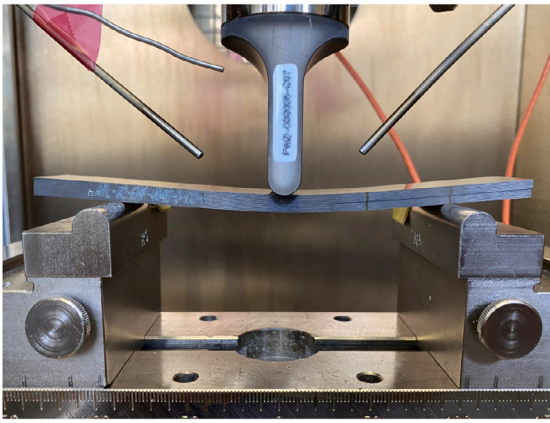


Fig. 8. ENF specimen inside 3-point bend setup according to ASTM D7905.



Fig. 9. MMB specimen inside fixture according to ASTM D6671.

speed of 0.5 mm/min. The crack length is defined by the distance from the insert foil to the closest bottom leg. Therefore, markings on the specimens are applied in order to facilitate installing of the specimen inside the 3-point bend setup and assure correct alignment. As crack propagation during ENF testing occurs abrupt, the crack propagation behaviour is not monitored and, therefore, no camera equipment is needed. One specimen of each test series is used to determine the correction parameters for the compact calibration (CC) method recommended in ASTM D7905. Therein, the second specimen in each series is loaded to 50% of the failure load of the respective interface for crack lengths of 15, 25 and 35 mm and force–displacement data is saved for the subsequent data reduction procedure.

The experimental setup of the MMB tests is shown in Fig. 9. The fixture used was manufactured according to ASTM D6671. A steel base bears the lower hinge clamp and the holder for the rear roller. The upper hinge clamp as well as the middle roller are connected to an aluminium lever. At the end of the lever a saddle is mounted which is moveable to adjust the mixed mode ratio. The load is introduced at this saddle via a loading yoke which is connected to the testing machine. A displacement is applied with a constant crosshead speed of 1 mm/min. Since only unstable crack propagation was observed the evolving crack distance was not recorded.

4.3. Data reduction methods

The data reduction methods proposed in the standards for DCB, ENF and MMB testing are adopted here for determination of the interlaminar properties. As previously described, mode interaction due to parasitic ERR effects are reduced by adjustment of the laminate layup. Therefore, perfectly isolated cERR modes are assumed within the application of the data reduction methods. However, the actual mode mixture in the different specimens is evaluated using numerical analysis with the VCCT to check if the assumptions of perfectly isolated modes holds true. The outcome is discussed in the results section. As recommended in ASTM D5528, data reduction of the DCB results is based on the modified beam theory (MBT). Therein, deviations from the beam theory due to rotation of the beams at the delamination front are taken into account by artificially increasing the delamination length $a + \Delta$.

According to ASTM D7905, the compact calibration (CC) method represents the only acceptable data reduction method for ENF testing. As described in the previous section, one specimen from each series is used to determine the CC coefficients by loading the specimen to 50% of the maximum force of a given interface at variable crack lengths a . Compliance of the specimen δ/P at different crack lengths of 15, 25 and 35 mm are then plotted over the respective cubed crack length a^3 , where the slope of the linear regression curve m represents the CC correction parameter.

For the data reduction of the MMB tests the procedure proposed in ASTM D6671 based on CBT is used. The ERR in mode I is calculated with the following equation:

$$G_I = \frac{12P^2(3c - L)^2}{16b^2h^3L^2E_{1f}}(a + \chi h)^2 \quad (21)$$

In mode II, the ERR can be calculated as follows:

$$G_{II} = \frac{9P^2(c + L)^2}{16b^2h^3L^2E_{1f}}(a + 0.42\chi h)^2 \quad (22)$$

In the equations above E_{1f} is the bending modulus of the laminate. With the two ERRs the total mixed mode ERR is determined with $G_T = G_I + G_{II}$. The mode mixture is then calculated by dividing the ERR in mode II with the total G_{II}/G_T . All ERRs described above can be calculated for any loading condition. However, delamination growth is associated with the cERR. These values are identified when the critical loading P_c is used instead of P . The ASTM standard describes three different ways to calculate P_c . In this work the most reproducible values $P_{5\%max}$ is chosen. The cERR of the corresponding DCB, ENF and MMB tests are then used to determine the interaction exponent η by a numerical curve fit of Eq. (9) using a python script.

5. Results and discussion

The following section covers the experimental as well as the numerical results and discussion of the multidirectional laminates under mode I, mode II and mixed mode loading. It is organised in subsections per mode respectively test type. In each mode specific subsection an overview of the derived fracture toughness values from each layup with a brief discussion is given first. This is followed by a detailed presentation and discussion of all performed investigations.

5.1. Mode I

The experimentally determined cERR values at crack initiation for the different interfaces considered, are presented in Table 2. Comparison of the cERR values reveals an effect of ply-angle difference on the interlaminar toughness of multidirectional interfaces. Starting from the $0^\circ//0^\circ$ interface with the lowest cERR, the interface toughness value at crack initiation increases slightly for the $0^\circ//45^\circ$ interface and reaches the highest values for $0^\circ//90^\circ$ and $45^\circ// -45^\circ$ interfaces, both having a ply-angle difference of 90° at the delamination plane.

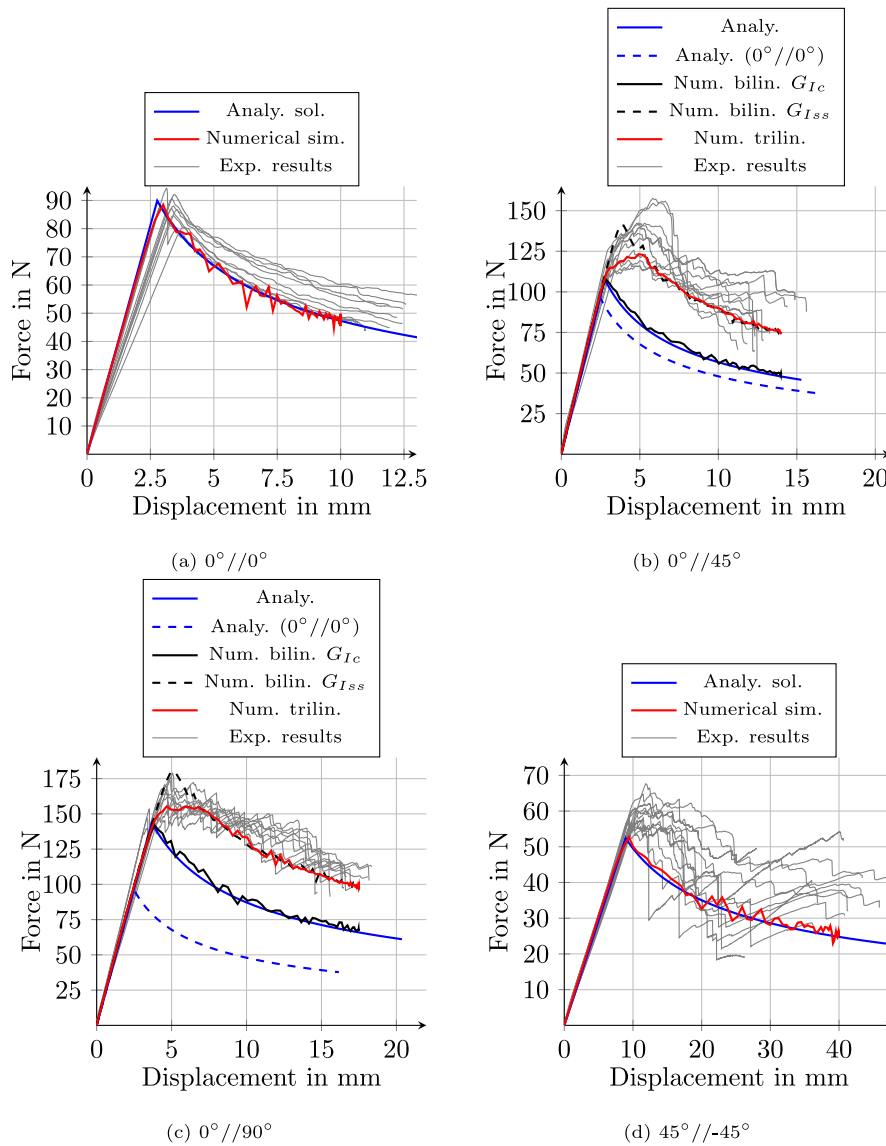


Fig. 10. Experimentally, analytically and numerically determined load–displacement curves of DCB test.

5.1.1. Experimentally determined force–displacement curves

The experimental force–displacement data of the DCB tests for 0°//0°, 0°//45°, 0°//90° and 45°//−45° interfaces are presented in Figs. 10(b)–10(d). While the 0°//0° interface exhibits a rather smooth decay in force after crack initiation indicating self-similar crack propagation, the behaviour of the 0°//45° and 0°//90° interfaces is characterised by an increase in force after crack initiation as well as crack propagation at an elevated load level indicating an R-curve behaviour. In case of the 45°//−45° interface, substantial scatter is present as soon as crack propagation is initiated. This behaviour is a result of significant fibre-bridging occurring during testing where the rip off of fibre bundles leads to severe and sudden load drops in the force–displacement curves.

5.1.2. R-curve behaviour

In Fig. 11 the evolution of the cERR with the crack extension Δa is shown for all four interfaces under investigation. In this plot the mean value at each crack extension is shown with an error bar to indicate the standard deviation. As can be expected from the characteristic behaviour of the force–displacement curves, the 0°//45° and 0°//90° interfaces exhibit an R-curve behaviour. For both interfaces a lower cERR at initiation increases until an elevated plateau is reached at

Table 2

Summary of calibrated mode I parameters.

Parameter	Unit	0°//0°	0°//90°	0°//45°	45°//−45°
n_{SP}	–	12	10	10	10
G_{Ic}	kJ/m ²	0.304	0.650	0.366	0.610
$\sigma_{G_{Ic}}$	kJ/m ²	±0.014	±0.164	±0.095	±0.138
$G_{I_{ss}}$	kJ/m ²	–	1.063	0.639	–
$\sigma_{G_{I_{ss}}}$	kJ/m ²	–	±0.109	±0.099	–
G_{I1}	kJ/m ²	–	0.650	0.366	–
G_{I2}	kJ/m ²	–	0.413	0.273	–
K_I	N/mm ³	10 ⁵	10 ⁵	10 ⁵	10 ⁵
K_{I1}	N/mm ³	–	9.5 · 10 ⁴	9.5 · 10 ⁴	–
K_{I2}	N/mm ³	–	5.0 · 10 ³	5.0 · 10 ³	–
T_n^0	MPa	20	20.0	20	20
T_{n1}^0	MPa	–	19.0	19.0	–
T_{n2}^0	MPa	–	1.0	1.0	–
m_I	–	–	0.61	0.57	–
n_I	–	–	0.95	0.95	–

crack extensions larger than 20 mm. The plateau can be interpreted as a steady state region with self-similar crack propagation behaviour.

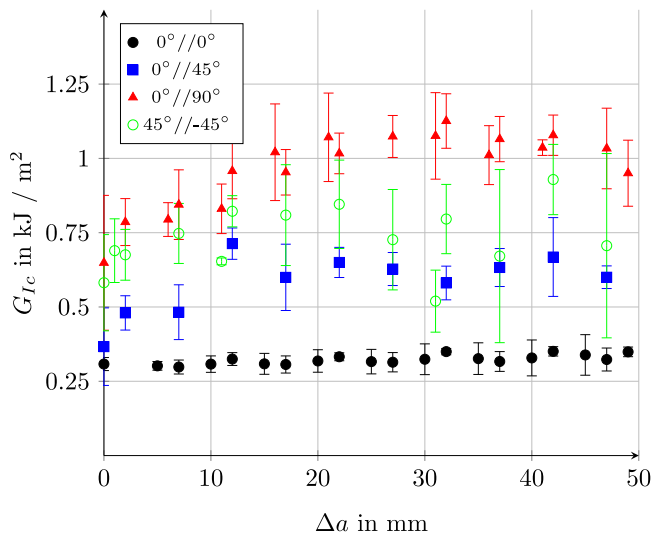


Fig. 11. Resistance curves of DCB tests with different interfaces (MBT).

The ERR at both, initiation and steady state conditions, exhibit some scatter, however, in average the behaviour is consistent. The cERR of the $0^\circ//45^\circ$ increases by 63.5% whereas the increase in cERR of the $0^\circ//90^\circ$ specimens is with 74.6% slightly larger. The cERR of the $45^\circ//−45^\circ$ specimens also increases. However, the effect is not as pronounced as with the interfaces discussed before and the cERR is affected with such a large scatter. The specimens with a standard $0^\circ//0^\circ$ -interface do not show any increase in cERR at all.

5.1.3. Analytical solutions

When comparing the experimentally determined force–displacement curves with the analytical solution based on the modified beam theory [35], agreement between the curves is very good for all interfaces up until crack initiation despite the fact that the analytical solution is derived for perfectly identical sublaminates. This assumption is strictly speaking not valid for the present laminate stackings. However, the comparison of analytical and experimental data indicates that the deviation in properties is negligible. When considering the crack propagation regime of the experimental force–displacement curves, only the $0^\circ//0^\circ$ interface exhibits self-similar crack propagation. Thus, the qualitative behaviour of analytical and experimental force–displacement curves is in agreement for that interface only. The remaining interfaces are all affected by fibre-bridging and crack-jumping to some extent. The analytical solution is not capable of accounting for such effects, thus, limiting its applicability to the behaviour up until crack initiation.

5.1.4. Numerical simulations

The simulation of the $0^\circ//0^\circ$ specimen according to ASTM D5528 using a bilinear traction–separation law is in good agreement with the experimental results, cf. Fig. 10(a). Since no R-curve behaviour was observed in the experiments, the superposition approach is not applied for this interface configuration.

For the $0^\circ//45^\circ$ specimens a distinct R-curve behaviour could be observed, cf. Fig. 11. Out of this reason several simulations were performed for this configuration. The two bilinear simulations show that, regardless of whether the initiation or the progression fracture toughness is used, the experimental curves cannot be reproduced satisfactorily, cf. Fig. 10(b). Using the initiation value the point of initiation is well met, but the progression is significantly underestimated. Using the steady-state progression fracture toughness the progression is well modelled, but the initiation is largely overestimated. The two trilinear simulations show that the superposition approach is able to capture the initiation as well as the progression behaviour. The simulation

using $n = 0.95$ fits qualitatively better than with $n = 0.90$. This is underlined by comparing the numerical to the experimental R-curves. Here, the steady-state phase is captured better by the simulation using $n = 0.95$. Again, bilinear simulation and analytical solution agree well. The analytical solution using the fracture toughness value of the “standard” $0^\circ//0^\circ$ -values shows that using the standard procedure for this interface configuration is conservative in terms of initiation as well as progression.

For the simulation of the $0^\circ//90^\circ$ specimens, the same observations apply as for the $0^\circ//45^\circ$ specimens. As can be seen in Fig. 10(c) in this case using the $0^\circ//0^\circ$ -value is even more conservative.

Since the analysis of the $45^\circ//−45^\circ$ R-curve did not reveal a distinct R-curve behaviour, this configuration was numerically analysed using the bilinear simulation approach only. As shown in Fig. 10(d) analytical and numerical solutions agree well. The initiation is captured with reasonable accuracy. However, the prediction of the progression is conservative. This could be attributed to the difficult parameter determination due to the large scatter in the experimental results.

It can be concluded that the strategies to estimate the interface stiffness and strength under consideration of the element size provides reasonable values which lead to satisfactory results. This holds true for all simulations performed. All mode I simulations show slight oscillations of the curve in the crack progression regime. This is attributed to the explicit integration scheme of the simulations.

5.1.5. Crack path and fracture surface

In order to assess crack jumping between adjacent interlaminar fracture planes, which is also called delamination migration, images of the fracture surfaces as well as from the crack paths are evaluated. Fig. 12 shows the conjugate post-mortem fracture surfaces of the top and bottom beam of one representative specimen of each interface configuration. In addition to the in-plane delaminations, in all four interfaces ripped off fibre bundles are visible. This means that all four interface configurations show crack propagation both within adjacent plies (intralaminar) and between adjacent plies (interlaminar), albeit to different degrees. The crack in the $0^\circ//0^\circ$ -specimen stays in the intended fracture plane. This is different for the test specimens with the $0^\circ//45^\circ$ interface shown. As can be seen in Fig. 12(b) starting from the insert the crack is intralaminar in the 45° -ply and then jumps to the $0^\circ//0^\circ$ interface in the lower beam and propagates in this interface with inter- as well as intralaminar shares. Again another behaviour can be observed in the $0^\circ//90^\circ$ -interface specimen, cf. 12(c). Here, the crack jumps through matrix cracks in the 90° -ply between the 0° -plies in the upper and lower beam. Fig. 12(d) shows a fracture surface of a $45^\circ//−45^\circ$ -specimen. There are two areas at the beginning and at the end which show large ripped of fibre bundles and interlaminar crack growths in between.

In addition to the fracture surfaces, Fig. 13 shows images taken from the side of one representative specimen for each interface during testing with significant crack extension. Overall, the findings in the crack paths images fit with the one from the fracture surfaces. The $0^\circ//0^\circ$ interface shows no noticeable jump in the crack plane and no fibre bundles. In the $0^\circ//45^\circ$ specimen a slight zigzag shape of the crack path as well as some fibre bundles can be observed. In the $0^\circ//90^\circ$ specimen, however, the zigzag shape of the crack path is strongly pronounced. This matches the fracture surface. The crack path, respectively side view of the $45^\circ//−45^\circ$ specimen also agrees with the fracture surface. At the beginning of the crack path some fibre bundles are visible but after that a smooth crack path without jumps is visible. At the crack tip in the image some fibre bundles maybe start to form again.

However, the evaluation of the Failure Modes by Cuntze reveal that in the simulation no fibre or interfibre failure is detected in the plies adjacent to the initial delamination plane, cf. Table 3. All stress efforts are significantly below 1.0, which would indicate a laminate failure. As expected the values for interfibre failure due to a tension load is the highest. The highest value is calculated for the $45^\circ//−45^\circ$ -interface

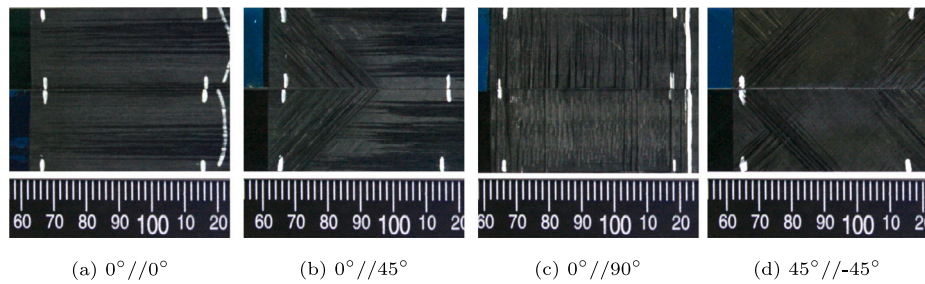


Fig. 12. Fracture surfaces of DCB specimens.

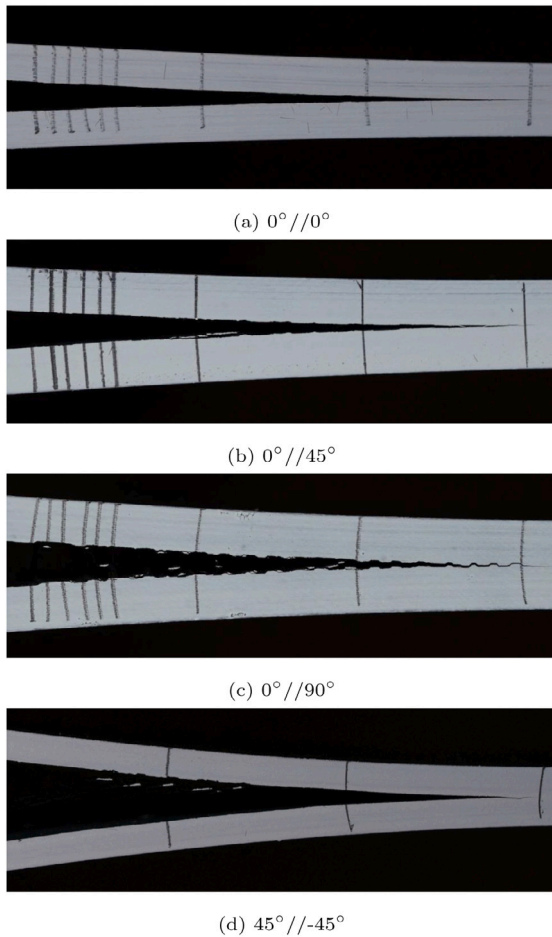


Fig. 13. Crack paths in DCB specimens.

with 0.42. This translates to a material stressing effort of 42% and underlines the need of effective properties in such simulations because matrix cracking with subsequent crack jumping cannot be captured in this kind of mesoscale simulations.

5.1.6. Crack front shape

Data reduction schemes and analytical solutions assume that the crack length is constant across the specimen width. This is not always the case in real tests. Urcelay [51] describes two kinds of deviations from a constant crack length across the width. First, the lack of uniformity which means that the crack lengths at the edges differ from the length in the middle. Second, the lack of symmetry which means that the crack length at the left and right edge differ. In this work, the crack front shape of the proposed layups is investigated for the DCB specimens with ultrasonic c-scan inspection, which is then

Table 3

Cuntze failure mode material stressing effort (DCB).

Interface	FF1	FF2	IFF1	IFF2	IFF3
0°//0°	0.10	0.00	0.21	0.04	0.06
0°//45°	0.12	0.00	0.27	0.04	0.12
0°//90°	0.14	0.01	0.38	0.05	0.05
45°//−45°	0.15	0.02	0.42	0.11	0.23

Table 4

Crack front shape: Distances of the right and left edges to the most advanced point of the crack front.

Interface	Left edge in mm	Right edge in mm
0°//0°	2.25	2.25
0°//45°	0.75	3.00
0°//90°	0.00	0.00
45°//−45°	3.00	3.00

compared with simulation results. The results are shown in Fig. 14. Blue elements show still fully bonded elements whereas red elements indicate completely degraded interfaces. The crack grows from right to left.

The crack fronts of the 0°//0° and 45°//−45° interfaces are both convex shaped meaning that the crack front in the middle of the specimen precedes. These crack fronts are non uniform but nearly symmetric. The crack front of the specimen with 0°//45° interface, on the other hand is inclined towards one end and therefore asymmetric. A straight crack front can be observed at the 0°//90° interface. In the ultrasonic C-scan image a partially weak echo indicates the pronounced delamination migration which is described in the previous section. All in all, a qualitative good agreement between simulation and ultrasonic inspection can be observed. Only the 0°//45° interface results in an asymmetric crack front. In future tests, this kind of specimen should be inspected from both sides during crack extension measurement. The crack front at the 45°//−45° interface is not significantly less uniform than the one of the standard 0°//0° interface. The quantitative measurements of the crack front shapes are taken from the simulations and summarised in Table 4. In summary, the chosen layups of the multidirectional specimens work satisfactorily.

5.1.7. Mode mixture

As described earlier the data reduction schemes as well as the analytical solutions assume perfectly isolated modes. However, multidirectional layups can lead to a mixed mode loading of the delamination plane. To check if the layups chosen with respect to a reduction of coupling work, VCCT analyses are performed to evaluate the mode mixture. The values reported in Table 5 are the observed maximum values along the width of the specimen and taken after the onset of delamination. The maximum values of the parasitic modes occurred at the free edges of the specimen. From the values, it can be concluded that in the DCB tests nearly pure mode I loading is achieved. The 0°//45° specimen shows the highest mode II and mode III components. However, these are with less than 3% from the average total cERR G_{tot}^{cav} negligible. This corresponds to the comparably low D_c and B_t values shown in Section 4.1.

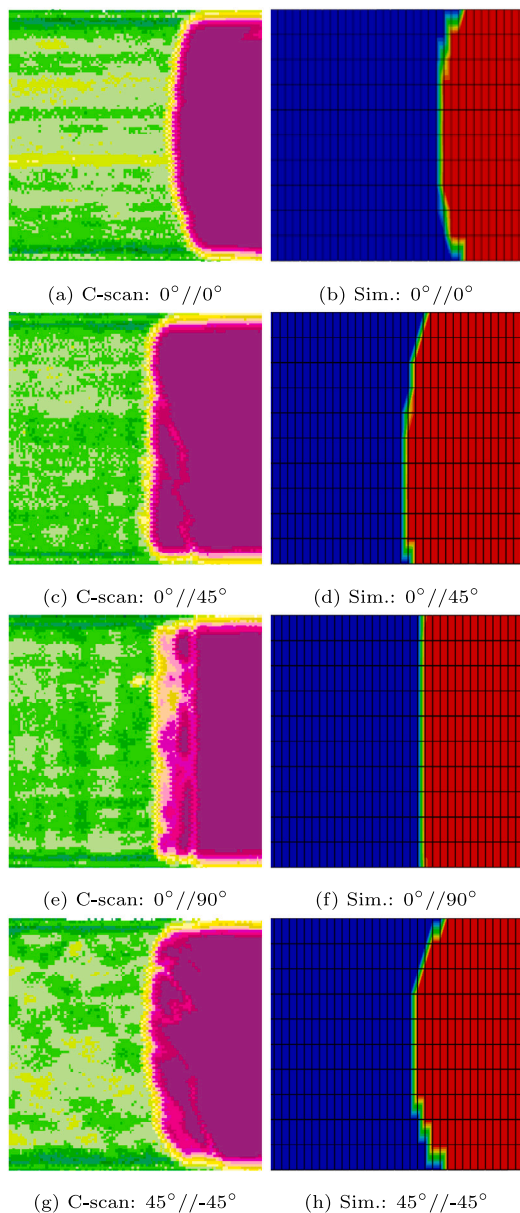


Fig. 14. Comparison of crack front shape from ultrasonic C-scan inspection and simulation results of DCB specimens. (For interpretation of the references to colour in this figure legend, the reader is referred to the web version of this article.)

Table 5
ERR components and mode mixture for different interfaces (DCB).

Interface	G_I (kJ/m ²)	G_{II} (kJ/m ²)	G_{III} (kJ/m ²)	G_{II}/G_{tot}^{av}	G_{III}/G_{tot}^{av}
0°//0°	0.333	0.000	0.000	0.000	0.000
0°//45°	0.402	0.009	0.004	0.022	0.010
0°//90°	0.712	0.005	0.004	0.007	0.006
45°//−45°	0.669	0.013	0.003	0.019	0.004

5.2. Mode II

In the following, the mode II results are presented and discussed in the same way as the mode I results before. Apart from the cERRs determined with the data reduction schemes discussed earlier, a summary of all mode II parameters used for the analytical and numerical analysis can be found in Table 6.

Similarly to the DCB results, the cERR of the 0°//0° interface is again the lowest and the interfaces with a ply-angle difference of

Table 6
Summary of calibrated mode II parameters.

Parameter	Unit	0°//0°	0°//90°	0°//45°	45°//−45°
n_{SP}	–	9	9	10	9
G_{IIC}	kJ/m ²	2.330	2.444	2.776	2.475
$\sigma_{G_{IIC}}$	kJ/m ²	±0.122	±0.139	±0.177	±0.103
K_{II}	N/mm ³	10 ⁵	10 ⁵	10 ⁵	10 ⁵
T_s^0	MPa	110.0	110.0	110.0	110.0

90° still produce similar cERR values, however, the behaviour of the 0°//45° interface brakes the pattern. Thus, contrary to the DCB results, no distinct dependency of the cERR in mode II on the difference in ply-angle between the interface layers can be observed.

5.2.1. Experimentally determined force–displacement curves

The force–displacement curves from the experimental ENF tests of the 0°//0°, 0°//45°, 0°//90° and 45°//−45° interfaces are presented in Fig. 15. Compared to the DCB results, the force–displacement curves in mode II exhibit more scatter with respect to both initial stiffness and initiation of crack propagation, possibly due to the manual alignment of the specimens in the 3-point bend setup during testing.

5.2.2. Analytical solutions

Good agreement between the experimental force–displacement curves and the analytical solution can be observed for the 0°//0° interface. In case of the remaining interfaces, agreement is less pronounced. While the analytically determined initial stiffness is slightly larger than the experimental stiffness of the 0°//45° and 0°//90° interfaces, the analytically determined initial stiffness in case of the 45°//−45° interface is considerably lower than in the experiment. Resulting from this difference in stiffness, the points of crack initiation in the force–displacement curves of the 0°//45°, 0°//90° and 45°//−45° interfaces are either slightly over- or underestimated.

5.2.3. Numerical simulations

In general, compared to the bilinear mode I simulations a lower agreement of the mode II simulations with the analytical solutions can be observed, cf. Figs. 15(a) to 15(d). The stiffness observed in the experiments is better captured by the numerical simulations than by the analytical solutions. All simulations except from the 0°//0° interface model the stiffness of the tests well until load drop. The simulation with the 0°//0° interface shows a nonlinearity prior to the load drop which cannot be observed in the experimental results. The forces and displacements at crack initiation also differ significantly between numerical and analytical solution. Again, the agreement with the experiment is better for the simulations. The crack initiation force is a bit low for the 0°//0° interface, but well captured for all other interfaces.

Since due to the unstable crack growth no R-curves were recorded during experimental testing, configurations are only modelled with the bilinear approach and not with a superposed trilinear traction–separation law. However, the bilinear approach works reasonably well in mode II. As observed in the mode I results the analytical solution using 0°//0°-values show that using this “standard” value is always conservative compared to the analytical solution with the interface specific value.

5.2.4. Fracture patterns

For the ENF specimens no side view images of the crack paths are available. However, the post-mortem fracture surfaces of the experimentally tested specimens, cf. Fig. 16, can be used in combination with the material stressing efforts summarised in Table 7. These material stressing efforts are calculated from the stresses determined with the numerical analyses in the plies adjacent to the intended fracture plane. The fracture surface of the specimen with the 0°//0° interface shows

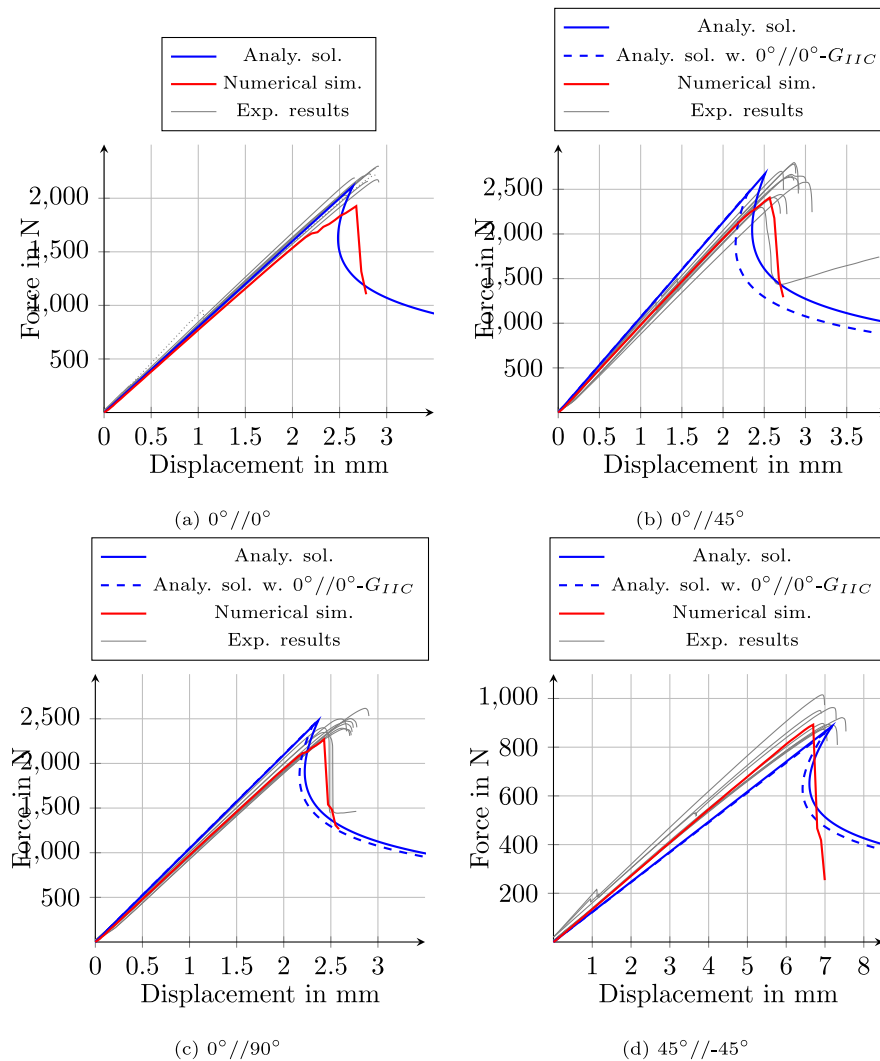


Fig. 15. Experimentally, analytically and numerically determined load–displacement curves of ENF tests.

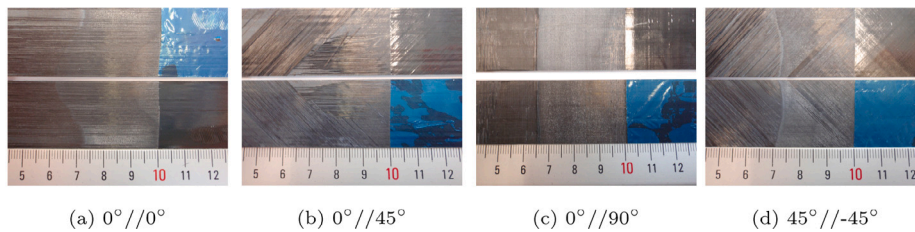


Fig. 16. Fracture surfaces of ENF specimens.

no delamination migration. However, some ripped off fibre bundles, which are attributed to fibre bridging, are visible. Different from that, the crack in the specimen with the $0^\circ//45^\circ$ interface grows at first interlaminar in the intended interface. With progressing crack growth intralaminar damage comes into play. At the end of testing the crack is completely migrated to an intralaminar crack in the 45° ply. The remaining interfaces show a much simpler fracture pattern. The crack in the $0^\circ//90^\circ$ specimen stays in the intended interface. The fracture surface of the $45^\circ//45^\circ$ specimen again shows some ripped off fibre bundles but all of them are oriented with 45° which lets the authors conclude that crack grows in the intended interface.

Unlike with the DCB specimens for every ENF specimen a failure mode reaches the value of 1.0, which means that a damage in the ply can be expected. The evaluation of the material stressing efforts for the $0^\circ//0^\circ$ results in an interfibre failure due to shear loading (IFF3) and for all other specimens in an interfibre failure due to tension loading (IFF1). This result supports the experimental observations.

5.2.5. Crack front shape

In Fig. 17 the crack front shapes determined by simulation for all four interfaces are shown. Except the specimen with the $45^\circ//45^\circ$ interface, all interfaces show a straight crack front which is uniform

Table 7
Cuntze failure mode material stressing effort (ENF).

Interface	FF1	FF2	IFF1	IFF2	IFF3
0°//0°	0.37	0.53	0.27	0.19	1.0
0°//45°	0.27	0.62	1.0	0.47	0.55
0°//90°	0.02	0.54	1.0	0.19	0.52
45°//−45°	0.34	0.48	1.0	0.67	0.58

Table 8
Highest (h) and in the middle (m) measured ERR components and mode mixture for different interfaces (ENF).

Interface	G_I (kJ/m ²)		G_{II} (kJ/m ²)		G_{III} (kJ/m ²)		G_I/G_{tot}^{av}		G_{III}/G_{tot}^{av}	
	h	m	h	m	h	m	h	m	h	m
0°//0°	0.017	0.003	2.533	2.088	0.774	0.000	0.007	0.001	0.306	0.000
0°//45°	0.017	0.001	3.048	2.971	1.556	0.000	0.006	0.000	0.510	0.000
0°//90°	0.001	0.000	3.045	2.854	0.640	0.000	0.000	0.000	0.210	0.000
45°//−45°	0.032	0.006	2.632	2.491	2.172	0.001	0.013	0.000	0.825	0.000

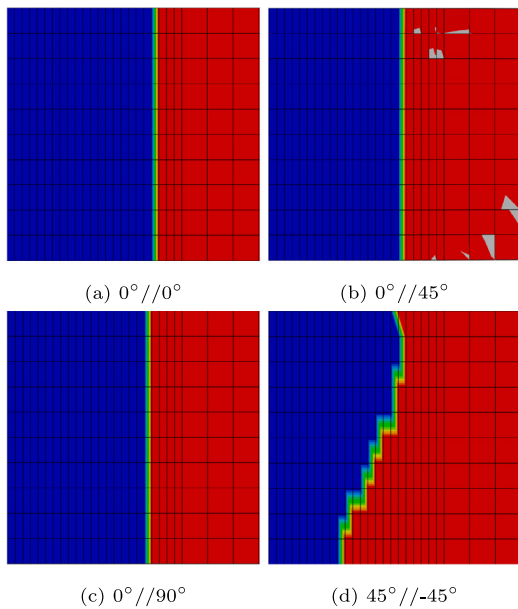


Fig. 17. ENF crack front shapes observed in numerical simulations.

and symmetric. The crack front in the 45°//−45° specimen is inclined and slightly curved. Therefore, it is non symmetric and non uniform.

5.2.6. Mode mixture

Like for the DCB specimen, again VCCT analyses are performed to determine the mode mixture for the different specimens. The highest values for each ERR component are shown in Table 8. The high mode I and mode III values occur in small regions from the edges towards the middle of the specimens, as also shown by Garulli et al. [25] for different layouts. As desired, mode I is small in every configuration. The highest mode I share can be found in the 45°//−45° specimen. However, with 1.3% it is rather small. Though, there are pronounced mode III components between 21% and up to 82.5%. Nevertheless, it needs to be mentioned that these high mode III components are very localised and even in the standard 0°//0° specimen there are areas with 30% mode III with respect to G_{tot}^{av} . The largest edge region with parasitic mode III fraction was observed in the 0°//45° specimen with 3 mm from the edge towards the centre of the specimen. As can be seen from Table 8 in the middle of the specimens pure mode II loading is achieved. Due to the small and local character of the parasitic modes, the authors assess the standard evaluation methods as applicable.

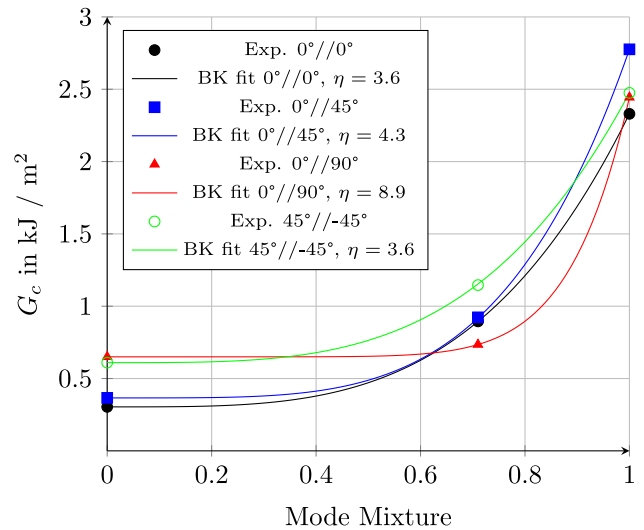


Fig. 18. Fracture toughness vs. mode mixture curves.

5.3. Mixed mode

MMB tests are used to determine G_T for an intended mixed mode ratio of 0.71. The 45°//−45° interface produces the highest G_T value with 1.146 kJ/m². Nearly the same cERR is determined for the 0°//0° and 0°//45° interfaces with 0.895 and 0.923 kJ/m². The 0°//90° interface results in the lowest cERR under the tested mixed mode loading ratio with 0.735 kJ/m². In Fig. 18 the cERR are shown together with the DCB and ENF results for all interfaces. When comparing the cERRs of the different test types respectively loading modes no clear trend of high and low cERR for the different interfaces can be observed. The 0°//90° interface for example shows the highest values in mode I, but the lowest under mixed mode conditions. Whereas for mode II loading the 0°//90° interface lies in the middle of the tested interfaces.

Using the DCB, ENF and MMB results a curve fit with a Python script was performed to find the exponent η of the BK law. The exponent is found to be the same for the 0°//0° and 45°//−45° interfaces with $\eta = 3.6$. The fitted value for the 0°//45° interface is with 4.3 comparable. With $\eta = 8.9$ a much higher η is determined for the 0°//90° interface. These values for η are used for the analytical and numerical analyses presented in the following.

5.3.1. Experimentally determined force–displacement curves

The force–displacement curves recorded during MMB testing are shown in Figs. 19(a) to 19(d). The experimentally determined curves of the specimens with 0°//0° and 0°//90° interfaces have the same characteristic shape. The force increases nearly linear until a small load drop occurs. After the load drop, the force rises again. This is different for the specimens with the 0°//45° interface where only a slight load drop is noticeable. The specimen with the 45°//−45° interface show no load drop at all. For this specimens a reproducible knee point with a change in stiffness can be observed. After the knee point the force increases slower.

5.3.2. Analytical solutions

The results of the analytical solution, cf. Figs. 19(a) to 19(d), can be summarised for all interfaces. The stiffness of experimental and analytical results are in good agreement until the load drop or change in stiffness in the experimental curves. However, the behaviour after this points is not well captured and the analytical solution overestimates the maximum forces in every case.

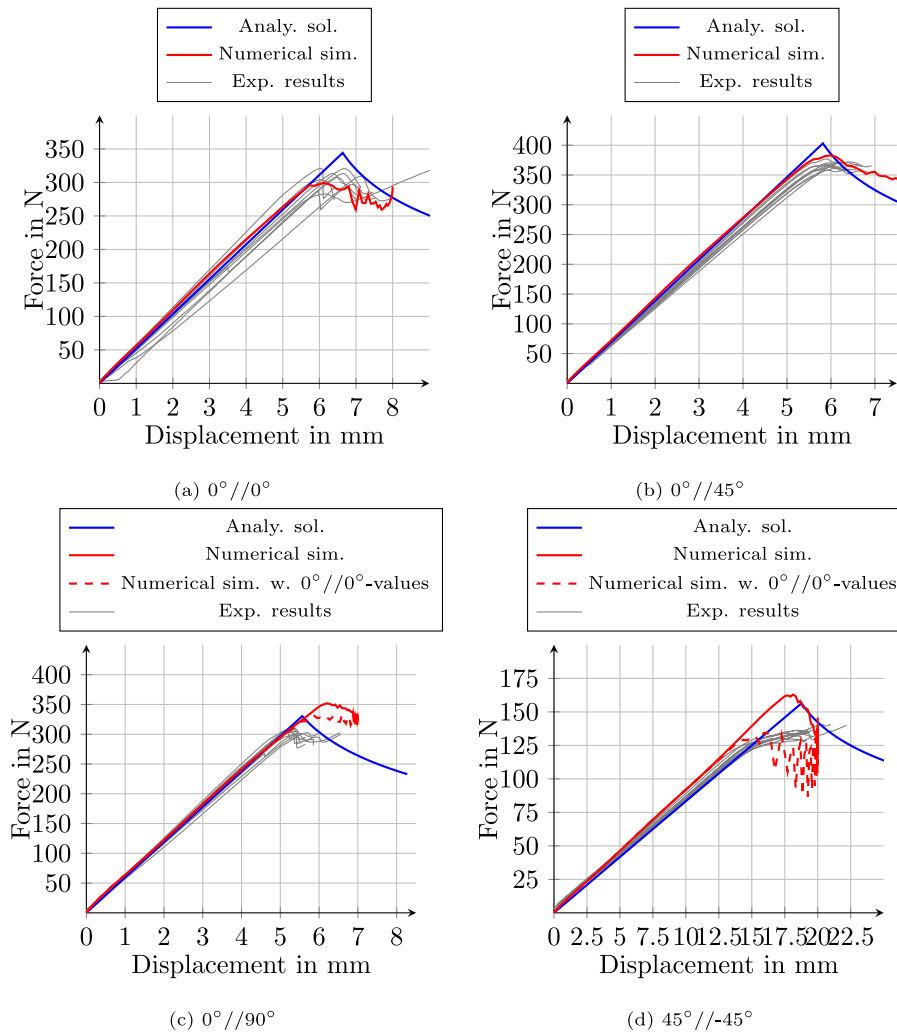


Fig. 19. Experimentally, analytically and numerically determined load–displacement curves of MMB tests.

5.3.3. Numerical simulations

Same as for the analytical solutions, the stiffness observed in the experiments is well modelled with numerical simulations. As can be seen in Figs. 19(a) and 19(b) there is a good agreement between numerical solutions and the experiment for the 0°//0° and 0°//45° interface both for crack initiation as well as progression. Compared to the experiment the maximum force for remaining two interfaces is overestimated compared to experiment, cf. Figs. 19(c) and 19(d). In addition, the shape of the force–displacement curve in the 45°//45° case is not well captured. There is a sudden load drop in the simulation results which could not be observed in the experiments. To check if the overestimation of maximum force in the 0°//90° case must be attributed to the interface specific values, a second simulation using the standard 0°//0° interface values was performed. This resulted in a slightly less but still existing overestimation. This leads the authors to the conclusion that the overestimation may be caused by damage processes in the real specimens which are not modelled in the numerical simulation. Hence, the 0°//90° and 45°//45° interfaces are the only cases, where the numerical simulation is less conservative than the analytical solution.

5.3.4. Fracture patterns

As with the ENF tests, only post-mortem images of the fracture surfaces are available for the MMB tests, cf. Fig. 20. In addition, like for DCB and ENF, the material stressing efforts of the plies adjacent to the intended fracture plane are given in Table 9. The fracture surfaces are

in general very comparable to the ones of the ENF specimens. The fracture surface of the 0°//0° interface shows no delamination migration. There are only some ripped off fibre bundles visible. Whereas the specimen with the 0°//45° interface first shows intralaminar crack growth in the 45° ply. With progressing growth the crack then migrates to an interlaminar crack respectively an intralaminar crack in the 0° ply. This is not totally clear. The fracture pattern of the 0°//90° specimen is significantly more uneventful. The crack stays in the intended interface. The last specimen type with the 45°//45° interface shows interlaminar crack growth in the intended interface but with some ripped off fibre bundles oriented under 45°. The findings from the fracture surfaces in general fit with the calculated material stressing efforts. For the 0°//0° specimen all stressing efforts are clearly below one which means no failure at all. For the 0°//45° again all failure modes are below one. However, the IFF1 effort is with 0.85 significantly closer to failure than with the 0°//0° specimen and in the fracture surface interfibre failures are visible. The next specimen with 0°//90° interface is predicted to have interfibre fractures, but the fracture pattern shows, at least no obvious interfibre failures. The highest stressing efforts overall are calculated for the 45°//45° specimen, but only the IFF1 value reaches 1. This fits to the ripped off fibre bundles visible in the fracture surface image.

5.3.5. Crack front shape

In all four simulations a straight and, therefore, uniform and symmetric crack front could be observed. Out of this reason the crack fronts are not shown in a figure.

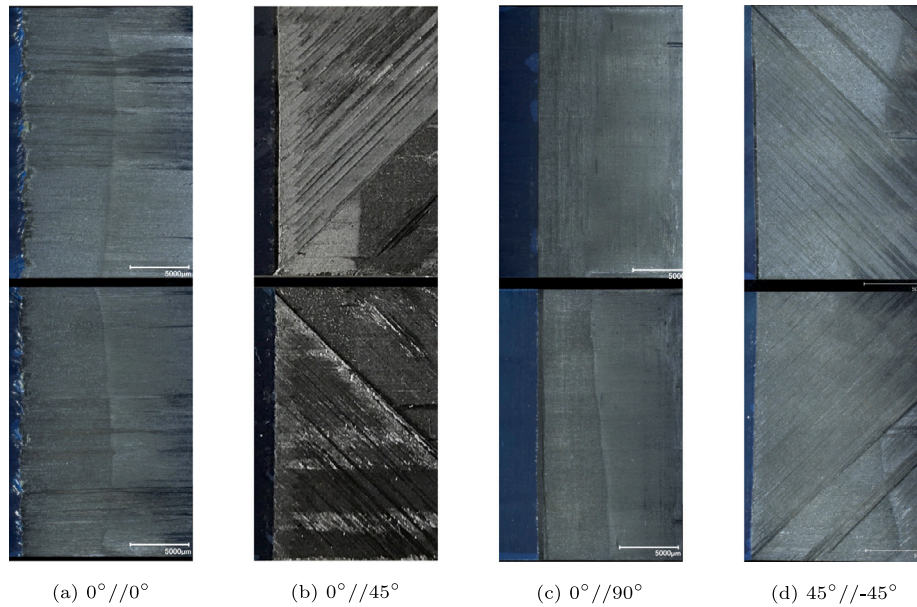


Fig. 20. Fracture surfaces of MMB specimens.

Table 9
Cuntze failure mode material stressing effort (MMB).

Interface	FF1	FF2	IFF1	IFF2	IFF3
0°//0°	0.31	0.20	0.25	0.08	0.42
0°//45°	0.16	0.00	0.85	0.06	0.37
0°//90°	0.04	0.20	1.00	0.05	0.40
45°//−45°	0.32	0.23	1.00	0.30	0.54

Table 10
Summary of calibrated M21-T700GC CZM parameters for different interfaces.

Property	0°//0°	0°//45°	0°//90°	45°//−45°	Unit
$K_I = K_{II} = K_{III}$			10 ⁵		N/mm ³
G_{Ic}	0.304	0.366	0.650	0.610	N/mm
$G_{IIc} = G_{IIIc}$	2.330	2.776	2.444	2.475	N/mm
T_I^0			20.0		MPa
$T_{II}^0 = T_{III}^0$			110.0		MPa
Initiation. criterion			QUADS		
Propagation criterion			BK		
η_{BK}	3.6	4.3	8.9	3.6	

5.3.6. Mode mixture

In this work, VCCT analyses are used to assess the parasitic modes in the test specimens with multidirectional layups. Since the mode mix of the MMB specimens lies between the DCB and ENF specimens, VCCT analyses were not performed for the MMB specimens.

5.4. Summary of interlaminar material properties

Table 10 summarises the determined interlaminar material properties of M21-T700GC for the different interfaces tested.

6. Conclusion

An experimental and numerical study on the influence of interface ply orientation on mode I, mode II and mixed-mode fracture toughness in multidirectional laminates has been conducted in this work. The effective fracture toughness of the same composite material largely depends on the interface orientations and can defer especially in Mode I by about 100%. Furthermore, the R-curve behaviour in mode I has been investigated. Whether an R-curve effect occurs or not depends on

interface orientation. R-curve behaviour in mode II and mixed-mode should be investigated in future work.

With respect to the numerical investigation, it was shown that the proposed procedure to reduce the mode I interface strengths to allow for larger elements is a valid approach. In addition, it could be shown that analytical solution and numerical results with bilinear traction–separation laws are in good agreement. The use of the 0°//0°-interface fracture toughness value for other interface orientations, the procedure according to the standards, results in very conservative predictions. In turn, the use of effective interface specific fracture toughness values improves simulation accuracy. Even though this way does not accurately describe the micromechanical physics, it can be a viable way for simulations in which interfibre failure is modelled using Continuum Damage Mechanics. Ultrasonic scans of the DCB specimens are used to compare the crack front shapes for validation. It can be shown that not only the load displacement curves of the characterisation specimens are well captured, but also the crack front shapes. This demonstrates that by smearing the microscale effects, the material behaviour can be captured phenomenologically correct by mesoscale modelling suitable for industrial use. Furthermore, it could be confirmed that superposition of two bilinear traction–separation laws to a trilinear law is a suitable solution to model R-curve behaviour. The validated set of physical and numerical parameters for the CFRP material M21-T700GC can be directly considered for delamination analysis of all composite structures made from this material.

Funding

Partial support for the work was provided by the German Federal Ministry For Economic Affairs And Energy, Germany within the collaborative project “Joining with predictable Damage Tolerance” - JoinDT (20W1918H).

Declaration of competing interest

The authors declare that they have no known competing financial interests or personal relationships that could have appeared to influence the work reported in this paper.

References

- [1] A.A. Griffith, The phenomena of rupture and flow in solids, *Philos. Trans. R. Soc. Lond. Ser. A Math. Phys. Eng. Sci.* 221 (-) (1920) 163–198.
- [2] ASTM, Standard test method for mode I interlaminar fracture toughness of unidirectional fiber-reinforced polymer matrix composites, 2001.
- [3] A. Pereira, A.B. Morais, Mode I interlaminar fracture of carbon/epoxy multidirectional laminates, *Compos. Sci. Technol.* 64 (-) (2004) 2267–2270.
- [4] ASTM, Test method for determination of the mode II interlaminar fracture toughness of unidirectional fiber-reinforced polymer matrix composites, 2014.
- [5] M.L. Benzeggagh, M. Kenane, Measurement of mixed-mode delamination fracture toughness of unidirectional glass/epoxy composites with mixed-mode bending apparatus, *Compos. Sci. Technol.* 56 (4) (1996) 439–449.
- [6] J.H. Crews, J.R. Reeder, A Mixed-Mode Bending Apparatus for Delamination Testing, National Aeronautics and Space Administration, Langley Research Center, 1988.
- [7] W.S. Johnson, P.D. Mangalgiri, Investigation of fiber bridging in double cantilever beam specimens: National aeronautics and space administration hampton VA langley research center.
- [8] Z. Suo, G. Bao, B. Fan, Delamination R-curve phenomena due to damage, *J. Mech. Phys. Solids* 40 (1) (1992) 1–16.
- [9] A.B. Pereira, A.B.d. Morais, M.d. Moura, A.G. Magalhães, Mode I interlaminar fracture of woven glass/epoxy multidirectional laminates, *Composites A* 36 (8) (2005) 1119–1127.
- [10] A.B. Pereira, A.B.d. Morais, A.T. Marques, P.T.d. Castro, Mode II interlaminar fracture of carbon/epoxy multidirectional laminates, *Compos. Sci. Technol.* 64 (10–11) (2004) 1653–1659.
- [11] J. Bieniasz, K. Dadej, B. Surowska, Interlaminar fracture toughness of glass and carbon reinforced multidirectional fiber metal laminates, *Eng. Fract. Mech.* 175 (2017) 127–145.
- [12] J. Andersons, M. König, Dependence of fracture toughness of composite laminates on interface ply orientations and delamination growth direction, *Compos. Sci. Technol.* 64 (13–14) (2004) 2139–2152.
- [13] C. Blondeau, G. Pappas, J. Botsis, Influence of ply-angle on fracture in antisymmetric interfaces of CFRP laminates, *Compos. Struct.* 216 (2019) 464–476.
- [14] Y. Gong, X. Chen, W. Li, L. Zhao, J. Tao, J. Zhang, N. Hu, Delamination in carbon fiber epoxy DCB laminates with different stacking sequences: R-curve behavior and bridging traction-separation relation, *Compos. Struct.* 262 (2021) 113605.
- [15] E.S. Greenhalgh, Failure Analysis and Fractography of Polymer Composites, in: Woodhead Publishing in Materials, Woodhead Pub., Cambridge, 2009.
- [16] A.B.d. Morais, A.B. Pereira, Mixed mode I+II interlaminar fracture of glass/epoxy multidirectional laminates – Part 1: Analysis, *Compos. Sci. Technol.* 66 (13) (2006) 1889–1895.
- [17] A.B. Pereira, A.B.d. Morais, Mixed mode I+II interlaminar fracture of glass/epoxy multidirectional laminates – Part 2: Experiments, *Compos. Sci. Technol.* 66 (13) (2006) 1896–1902.
- [18] S. Bennati, M. Colleluori, D. Corigliano, P.S. Valvo, An enhanced beam-theory model of the asymmetric double cantilever beam (ADCB) test for composite laminates, *Compos. Sci. Technol.* 69 (11–12) (2009) 1735–1745.
- [19] S. Bennati, P. Fissicaro, P.S. Valvo, An enhanced beam-theory model of the mixed-mode bending (MMB) test—Part II: Applications and results, *Meccanica* 48 (2) (2013) 465–484.
- [20] B. Davidson, R. Krüger, M. König, B.D. Davidson, Effect of stacking sequence on energy release rate distribution in multidirectional DCB and ENF specimens - effect of stacking sequence on energy release rate distributions in multidirectional dcb and enf specimens, *Eng. Fract. Mech.* 55 (4) (1996) 557–569.
- [21] P. Prombut, L. Michel, F. Lachaud, J. Barrau, Delamination of multidirectional composite laminates at 0/Theta ply interfaces, *Eng. Fract. Mech.* 73 (-) (2006) 2427–2442.
- [22] J. Tao, C. Sun, J. Tao, C.T. Sun, Influence of ply orientation on delamination in composite laminates, *J. Compos. Mater.* 32 (21) (1998//2016) 1933–1948.
- [23] N. Choi, A. Kinloch, J. Williams, Delamination of multidirectional carbon-fiber / epoxy composites under mode I, mode II and mixed-mode I-II loading, *J. Compos. Mater.* (-) (1999) 73–101.
- [24] T. Garulli, A. Catapano, D. Fanteria, W. Huang, J. Jumel, E. Martin, Experimental assessment of fully-uncoupled multi-directional specimens for mode I delamination tests, *Compos. Sci. Technol.* 200 (2020) 108421, <http://dx.doi.org/10.1016/j.compscitech.2020.108421>.
- [25] T. Garulli, A. Catapano, D. Fanteria, J. Jumel, E. Martin, Design and finite element assessment of fully uncoupled multi-directional layouts for delamination tests, *J. Compos. Mater.* 54 (6) (2020) 773–790, <http://dx.doi.org/10.1177/0021998319868293>.
- [26] T. Garulli, A. Catapano, M. Montemurro, J. Jumel, D. Fanteria, Quasi-trivial stacking sequences for the design of thick laminates, *Compos. Struct.* 200 (2018) 614–623, URL <https://hal.archives-ouvertes.fr/hal-02354468>.
- [27] A. De Morais, M.F. De Moura, Evaluation of initiation criteria used in interlaminar fracture tests, *Eng. Fract. Mech.* 73 (16) (2006) 2264–2276.
- [28] P.P. Camanho, C.G. Davila, M. De Moura, Numerical simulation of mixed-mode progressive delamination in composite materials, *J. Compos. Mater.* 37 (16) (2003) 1415–1438.
- [29] R. Krueger, Virtual crack closure technique: history, approach, and applications, *Appl. Mech. Rev.* 57 (2) (2004) 109–143.
- [30] S. Karmakov, F. Cepero-Mejías, J. Curiel-Sosa, Numerical analysis of the delamination in CFRP laminates: VCCT and XFEM assessment, *Composites C* 2 (2020) 100014.
- [31] M. Heidari-Rarani, M. Sayedain, Finite element modeling strategies for 2D and 3D delamination propagation in composite DCB specimens using VCCT, CZM and XFEM approaches, *Theor. Appl. Fract. Mech.* 103 (2019) 102246.
- [32] C.G. Dávila, C.A. Rose, P.P. Camanho, A procedure for superposing linear cohesive laws to represent multiple damage mechanisms in the fracture of composites, *Int. J. Fract.* 158 (2) (2009) 211–223.
- [33] A. Turon, C.G. Davila, P.P. Camanho, J. Costa, An engineering solution for mesh size effects in the simulation of delamination using cohesive zone models, *Eng. Fract. Mech.* 74 (10) (2007) 1665–1682.
- [34] X. Lu, M. Ridha, B. Chen, V. Tan, T. Tay, On cohesive element parameters and delamination modelling, *Eng. Fract. Mech.* 206 (2019) 278–296.
- [35] P.W. Harper, S.R. Hallett, Cohesive zone length in numerical simulations of composite delamination, *Eng. Fract. Mech.* 75 (16) (2008) 4774–4792.
- [36] A. Hillerborg, M. Modéer, P.-E. Petersson, Analysis of crack formation and crack growth in concrete by means of fracture mechanics and finite elements, *Cem. Concr. Res.* 6 (6) (1976) 773–781.
- [37] Q. Yang, B. Cox, Cohesive models for damage evolution in laminated composites, *Int. J. Fract.* 133 (2) (2005) 107–137.
- [38] E. Petersen, E. Kappel, J. Koord, O. Völkerink, C. Hühne, Determination of stresses, strains and failure types in multidirectional laminates under pure bending, *J. Compos. Mater.* (2020) 0021998320932301.
- [39] O. Völkerink, E. Petersen, J. Koord, C. Hühne, A pragmatic approach for a 3D material model considering elasto-plastic behaviour, damage initiation by puck or cuntze and progressive failure of fibre-reinforced plastics, *Comput. Struct.* 236 (2020) 106280.
- [40] W. Cui, M. Wisnom, M. Jones, A comparison of failure criteria to predict delamination of unidirectional glass/epoxy specimens waisted through the thickness, *Composites* 23 (3) (1992) 158–166.
- [41] P.P. Camanho, C.G. Dávila, Mixed-mode decohesion finite elements for the simulation of delamination in composite materials, 2002.
- [42] A. De Morais, Cohesive zone beam modelling of mixed-mode I-II delamination, *Composites A* 64 (2014) 124–131.
- [43] A. Turon, P.P. Camanho, J. Costa, C. Dávila, A damage model for the simulation of delamination in advanced composites under variable-mode loading, *Mech. Mater.* 38 (11) (2006) 1072–1089.
- [44] E.M. Wu, R. Reuter Jr., Crack Extension in Fiberglass Reinforced Plastics, Tech. rep., Illinois Univ at Urbana Dept of Theoretical and Applied Mechanics, 1965.
- [45] R. Gutkin, M. Laffan, S. Pinho, P. Robinson, P. Curtis, Modelling the R-curve effect and its specimen-dependence, *Int. J. Solids Struct.* 48 (11–12) (2011) 1767–1777.
- [46] A. Airoidi, C.G. Dávila, Identification of material parameters for modelling delamination in the presence of fibre bridging, *Compos. Struct.* 94 (11) (2012) 3240–3249.
- [47] C.G. Davila, F.A. Leone, K. Song, J.G. Ratcliffe, C.A. Rose, Material characterization for the analysis of skin/stiffener separation, 2017.
- [48] D. Ranz, J. Cuartero, L. Castejón, R. Miralbes, D. Valladares, Enhanced cohesive zone model to predict delamination behavior of carbon/epoxy laminated curved beams, *Mech. Adv. Mater. Struct.* (2020) 1–11.
- [49] A.d. Morais, Beam analysis of the double cantilever beam specimen with fibre bridging, *J. Compos. Mater.* 49 (14) (2015) 1681–1688.
- [50] L. Zhao, Y. Gong, J. Zhang, Y. Chen, B. Fei, Simulation of delamination growth in multidirectional laminates under mode I and mixed mode I/II loadings using cohesive elements, *Compos. Struct.* 116 (2014) 509–522.
- [51] I. Urcelay Oca, Experimental Determination of Fracture Toughness for Delamination Analysis in Structural Components (Master's thesis), TU Delft, 2020.
- [52] A. Raimondo, I. Urcelay Oca, C. Bisagni, Influence of interface ply orientation on delamination growth in composite laminates, *J. Compos. Mater.* (2021) 00219983211031636.
- [53] F. Daricik, Mesh size sensitivity analysis for interlaminar fracture of the fiber-reinforced laminated composites, *J. Eng. Fibers Fabrics* 14 (2019) 1558925019883460.
- [54] E. Petersen, R. Cuntze, C. Hühne, Experimental determination of material parameters in Cuntze's failure-mode-concept-based UD strength failure conditions, *Compos. Sci. Technol.* 134 (2016) 12–25.
- [55] T. Sebaey, N. Blanco, C. Lopes, J. Costa, Numerical investigation to prevent crack jumping in double cantilever beam tests of multidirectional composite laminates, *Compos. Sci. Technol.* 71 (13) (2011) 1587–1592.
- [56] A. de Morais, A. Pereira, Interlaminar fracture of multidirectional glass/epoxy laminates under mixed-mode I+ II loading, *Mech. Compos. Mater.* 43 (3) (2007) 233–244.
- [57] P. Robinson, D. Song, A modified DCB specimen for mode I testing of multidirectional laminates, *J. Compos. Mater.* 26 (11) (1992) 1554–1578.